Soft Matter

Accepted Manuscript

ROYAL SOCIETY OF CHEMISTRY

www.rsc.org/softmatter

ARTICLE TYPE www. rsc.org/xxxxxx | XXXXXXXX

Oil Diffusivity through Fat Crystal Networks†

Nicole L. Green[a] **and Dérick Rousseau***[a]

Received Xth XXXXXXXXXX 20XX, Accepted Xth XXXXXXXXX 20XX
First published on the web Xth XXXXXXXXXX 200X
DOI: 10.1039/b000000x

Oil migration in chocolate and chocolate-based confections leads to undesirable visual and textural changes. Establishing ways to slow this unavoidable process would increase shelf life and reduce consumer rejection. Diffusion is most often credited as the main pathway by which oil migration occurs. Here, we use fluorescence recovery after photobleaching (FRAP) to explore the diffusion coefficients of vegetable and mineral oil through fat crystal networks at different solid fat contents (SFC). Differences in compatibility between the fat and oil lead to unique primary crystal clusters, yet those variations do not affect diffusion at low SFCs. Trends deviate at higher SFCs, which we ascribe to the influence of the differing crystal cluster structures. We relate our results to the strong and weak-link rheological regimes of fat crystal networks. Finally, we connect the results to relationships developed for polymer gel systems.

1 Introduction

Developing an understanding of the oil migration rate and mechanism in food systems is of industrial importance. Diffusion based on triacylglycerol (TAG) concentration gradients is often cited as one cause of oil migration in chocolate and chocolate-coated confections.[1–3] Oil migration leads to visual and textural changes such as fat bloom, eventually resulting in consumer rejection. Chocolate is a complex mixture of oil-impermeable solid particles, liquid oil, and solid fat, so it is difficult to devise a mechanism that can account for its structural heterogeneities. Variables such as chemical composition and storage temperature will also affect the rate and extent of oil migration, further complicating the problem.

Techniques to visualize oil uptake into a solid fat matrix include magnetic resonance imaging[4,5] and scanning of fluorescently labeled oil,[6] both which correlate signal values with liquid oil content. Molecular-based methods like gas-liquid chromatography[7,8] or high performance liquid chromatography[9] quantify the oil migration by exploiting differences in fatty acid distribution between the oil and fat components. Alone, these methods do not provide structural information, so they are often used with X-ray diffraction (XRD),[10] pulsed nuclear magnetic resonance (pNMR),[11] atomic force microscopy (AFM),[9] scanning electron microscopy (SEM),[12] confocal laser scanning microscopy (CLSM),[13] or polarized light microscopy (PLM).[10] Structural information can be on the nanoscale (polymorphic form – XRD) or microscale (crystal shape and size – PLM, topological features – AFM and SEM). Most experimental oil migration data are then compared to a simplified solution to Fick's second law of diffusion[14]

$$\frac{M_t}{M_\infty} = \frac{A\sqrt{Dt}}{V} = \sqrt{\frac{Dt}{l^2}} \quad (1)$$

where A is the contact area between the chocolate and the foreign oil source, V is the chocolate volume, and l is the diffusion path length. If the system is a layered chocolate and filling confection, the second expression is appropriate whereas the third is more suitable for a pure chocolate system in which a value for contact area is not applicable. Assuming Equation 1 holds true, one can use experimental measurements of time-dependent oil migration M_t and M_∞ to predict the diffusion coefficient D or vice versa. If there existed a method to accurately calculate diffusion coefficients, those could then be used to estimate the extent of oil migration of an unknown sample.

A technique capable of measuring the local diffusion coefficient is fluorescence recovery after photobleaching (FRAP).[15] It is a microscopy-based technique that measures the diffusion of dye molecules into a bleached region by monitoring the fluorescence recovery. Assuming that the dye and oil move in tandem, the rate of intensity recovery is the same as the rate of molecular diffusion. FRAP has largely been used in biological systems to study the mobility and binding interactions of fluorescent proteins *in vivo*.[16–18] It has been used sparingly in food systems, namely in starch solutions,[19] model cheeses,[20,21] fat crystal networks,[6] and model chocolates.[22] It is applicable to heterogeneous food systems and can measure differences in diffusivities based on crystal size and structure but has not been shown to be sensitive to the inclusion of impermeable solid particles.[23] Often FRAP experiments use different sizes

† Electronic Supplementary Information (ESI) available: [Solid fat content measurements and postbleaching profile along the optical axis]. See DOI: 10.1039/b000000x/

[a] *Department of Chemistry and Biology, Ryerson Unviersity, Toronto, ON, Canada. E-mail: rousseau@ryerson.ca*

of fluorescent probes to study the transport properties of a matrix.[20,24] In this study, we used FRAP to calculate the local diffusion coefficients of a hard fat mixed with vegetable or mineral oil as a function of solid fat content (SFC), SFC being simple to determine experimentally. We then fit the diffusivity results to empirical relationships from polymer gelation experiments. Results show evidence of a nonlinear relationship between diffusivity and SFC with three distinct SFC-dependent regimes.

2 Methods

2.1 Sample preparation

Mixtures of hydrogenated canola oil (HCO, Bunge, Oakville, ON, Canada) and either canola oil (CO, Selection, Toronto, ON, Canada) or light mineral oil (LMO, Fisher Scientific, Whitby, ON, Canada) were prepared at room temperature, with all ratios reported as mass ratios (w/w). The blend compositions ranged from 0/100 to 80/20. Separately, the lipophilic fluorochrome fluorol yellow 088 (Sigma-Aldrich, St. Louis, MO, USA) was dissolved in either CO or LMO and added to the mixtures to yield a final concentration of 1500 µmol/L.[6] Samples were kept at 100°C for 20 minutes and vortexed throughout to blend the mixtures. Unused stock solutions were sealed in airtight containers, kept in the dark, and used within a week of initial preparation. Once mixed, samples were immediately loaded into heated microscope slide and cover glass chambers that were approximately $15 \times 8 \times 0.15$ mm. They were sealed with epoxy to minimize air exposure. Chambers were then heated to 90°C, held there for 20 minutes, then returned to room temperature at 5°C/min. FRAP samples were used 2 – 12 hours after preparation depending on the HCO concentration, higher requiring longer time for dye concentration to equilibrate.

2.2 Imaging equipment

All FRAP experiments were conducted on a Zeiss LSM510 confocal laser scanning microscope (Zeiss Inc., Toronto, ON, Canada) with a 10× (0.25 NA) objective. All data were taken at room temperature and at a frame size of 153.6×153.6 µm, captured at a resolution of 128×128 pixels. Both bleaching and imaging were carried out with the 488 nm wavelength of a 40 mW argon laser; the laser power was set to 100% for bleaching and the minimum (25%) for imaging. Further, the 488 nm line was set to 100% for bleaching and between 0.5 – 5%, depending on the specific sample brightness, for imaging. For FRAP, the beam path was equipped with an HFT 488/543 dichroic beam splitter and an LP 505 emission filter. The pinhole was set to 1 Au, leading to an optical thickness of < 16.8 µm. Separately, data with a maximum pinhole size were collected to compare results – see supplemental information. In addition, polarized light images were taken on a Zeiss Axiovert-200M inverted light microscope (Zeiss Inc., Toronto, ON, Canada) with a 63× (1.40 NA) objective and 0.50 NA condenser. Those images were acquired with a QImaging Retiga-4000R digital camera (QImaging, Surrey, BC, Canada).

2.3 FRAP protocol

FRAP experiments can be divided into three sections: prebleaching, bleaching, and postbleaching. The scan rate, or time a frame was illuminated, was held constant at 147.46 ms/frame, while the frame rate, or the time between subsequent frames, was varied but never faster than 1 frame/s during postbleaching. Samples are only exposed to laser light during image capture. Here, the prebleaching step consisted of 12 images taken at the maximum frame rate. The bleached region was a centrally-located circle with radius $\omega_B = 36$ µm. The bleaching program only illuminated the specified region so the surrounding area remained unaffected. Bleaching scanned this region 25 – 70 times, lasting between 1.7 – 4.8 seconds, at least maintaining the recommended 15:1 ratio between recovery and bleaching time.[25] The postbleaching duration depended on the sample specifics, but all were collected until full recovery.

2.4 FRAP analysis

Raw image stacks were analyzed using ImageJ software (National Institute of Health, Bethesda, MD, USA, http://imagej.nih.gov/ij/). The mean intensity $F_{ROI}(t)$ within a centered region of interest (ROI) of radius $\omega_{ROI} = 28.8$ µm was determined as a function of time. Note that $\omega_{ROI} < \omega_B$ to exclude any effect from diffusion during the bleaching pulse, which would blur the edges of the bleach spot depending on the bleaching duration and the recovery rate. The intensity within the ROI was normalized against the mean background intensity $F_{bkg}(t)$, defined as the intensity outside a circle of radius $\omega_{bkg} = 81.6$ µm, as shown in Figure 1. Without this normalization, any wholesale changes in image intensity could lead to arbitrary fluctuations in mean intensity. The background intensity was unaffected by the recovery (see supplemental information), so this normalization did not skew the results. Data were then normalized by the mean prebleach intensity, defined as the intensity within the ROI from the prebleach frames, designated as $F_{ROI}(t_i^-)$:

$$\hat{F}(t) = \frac{F_{ROI}(t)/F_{bkg}(t)}{\sum_{i=1}^{12} F_{ROI}(t_i^-)} \quad (2)$$

The recovery curve $f(t)$ was written as

$$f(t) = \frac{\hat{F}(t) - \alpha\hat{F}(0)}{\hat{F}(\infty) - \alpha\hat{F}(0)} \quad (3)$$

where $\alpha = \hat{F}(0)/\hat{F}(t^-)$, $t = 0$ signifies the first postbleach frame, and $\hat{F}(\infty)$ is averaged from the data after intensity has reached its plateau value. The recovery curves were fitted to the 2D formula for a uniform disk bleached by a scanning beam[26]

$$f_k(t) = a + \sum_{n=1}^{\infty} \frac{(-K_0)^n}{n!\sqrt{1+n}} \left(1 - e^{-2\tau/t}\left[I_0\left(\frac{2\tau}{t}\right) + I_1\left(\frac{2\tau}{t}\right)\right]\right) \quad (4)$$

where K_0 is the bleaching depth parameter, a is a fitting parameter to account for the possibility of any immobile fraction, and $\tau = \omega_{ROI}^2/4D$ is the radial diffusion time. If $a = 1$ then there is no immobile fraction. We adjust ω_B via $\Delta\omega/r_0 = -0.0106K_0^2 + 0.163K_0$ where r_0 is the axial resolution if $K_0 > 2$.[26] Experimental parameters were determined by a nonlinear least squares fit to Equation 3 with Matlab (R2014a, Mathworks, Natick, MA, USA). We used the 2D formula because the objective NA is small, making the bleach profile cylindrical within the bleach volume. This analysis was repeated in at least three different locations with the resulting D values averaged. An example of the normalized data and fit to Equation 4 is shown in Figure 2.

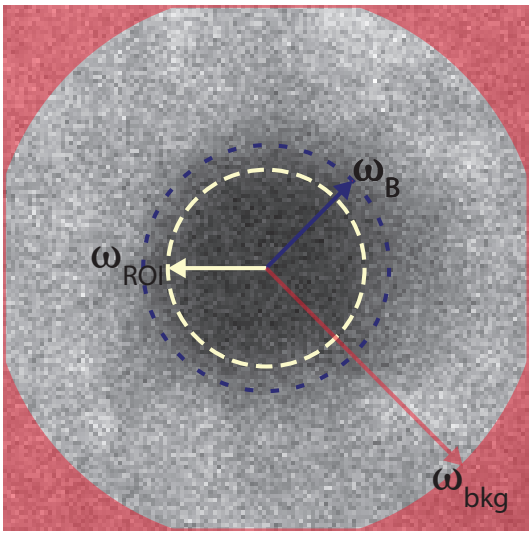

Fig. 1 First postbleaching frame of a 40/60 (w/w) HCO/LMO sample. The short dashed path encircles the bleached area, while the long dashed path indicates the area used to calculate $F_{ROI}(t)$. The shaded corners are used to calculate $F_{bkg}(t)$.

2.5 Solid fat content measurements

SFC was measured via pulsed nuclear magnetic resonance (pNMR) using a Bruker Minispec Mq system (Bruker Canada, Milton, ON, Canada) and the sfc_lfc application (v2.51). Mixtures of HCO and either CO or LMO were weighed into glass NMR tubes, melted at 90°C for 20 minutes, and then cooled at 5°C/min back to room temperature. This cooling protocol was chosen to match that of the microscope slides. Measurements were performed in triplicate.

2.6 Viscosity measurements

Viscosities of 100% CO and LMO were measured at 25°C with a rheometer (MCR 301, Anton Paar, Ville St-Laurent, QC, Canada) equipped with a cup and bob geometry (CC27). Stress measurements were plotted as a function of strain rate between 1 – 100 s^{-1} to calculate viscosity. Viscosity values were averaged over three runs.

2.7 X-ray diffraction

Small and wide-angle x-ray diffraction (SAXD and WAXD) of the fat/oil mixtures were collected using a Hecus S3-MICROcaliX high flux system (Hecus, Graz, Austria). The unit uses a 5 W, high brilliance GeniX microfocus source and customized FOX-3D multi-layer point focusing optics (Xenocs SA, Grenoble, France) with a 100×250 μm^2 FWHM (vertical $\times$ horizontal) at focus. The x-ray beam was generated by a 50 kV, 1 mA CuK_α anode. The sample-detector distance was 280 mm. Spectra were captured with dedicated Hecus 1-D position-sensitive detectors (model PSD-50M). For sample preparation, 20 µL of melted sample were placed in 1.0 mm O.D. quartz capillaries (Charles Supper Company, Inc., Natick, MA, USA) using a long needle and syringe. Samples were melted at 90°C and quickly cooled to room temperature, where they remained for three hours prior to data collection. Peak analysis was performed using OriginPro8 software (OriginLab, Northampton, MA, USA). Thickness (th) was calculated using the Scherrer equation[27]

$$\text{th} = \frac{0.9\lambda}{\text{FWHM}\cos\theta} \quad (5)$$

where λ is the X-ray wavelength (CuK_α radiation, $\lambda = .15406$ nm), θ is the diffraction angle, and FWHM is the full width at half the maximum of the Gaussian fitting to the peak. Data were collected and analyzed in triplicate.

3 Results and Discussion

From FRAP, the diffusion coefficient values for the 100% liquid systems, D_0, were 1.37×10^{-11} m^2/s for CO and

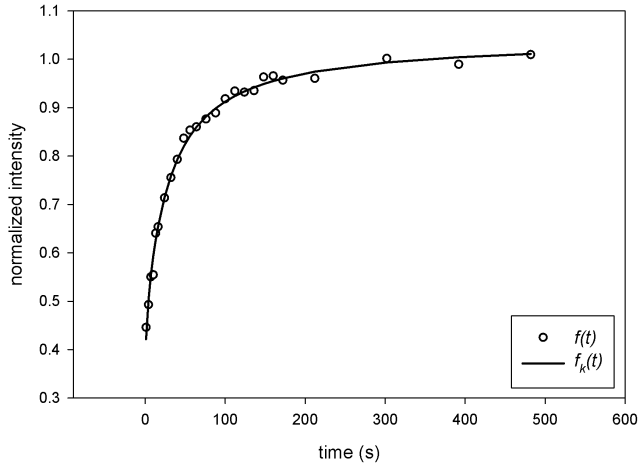

Fig. 2 20/80 (w/w) HCO/CO normalized data: points denote recovery data $f(t)$ according to Equation 3 as a function of time, while line $f_k(t)$ is fit to data.

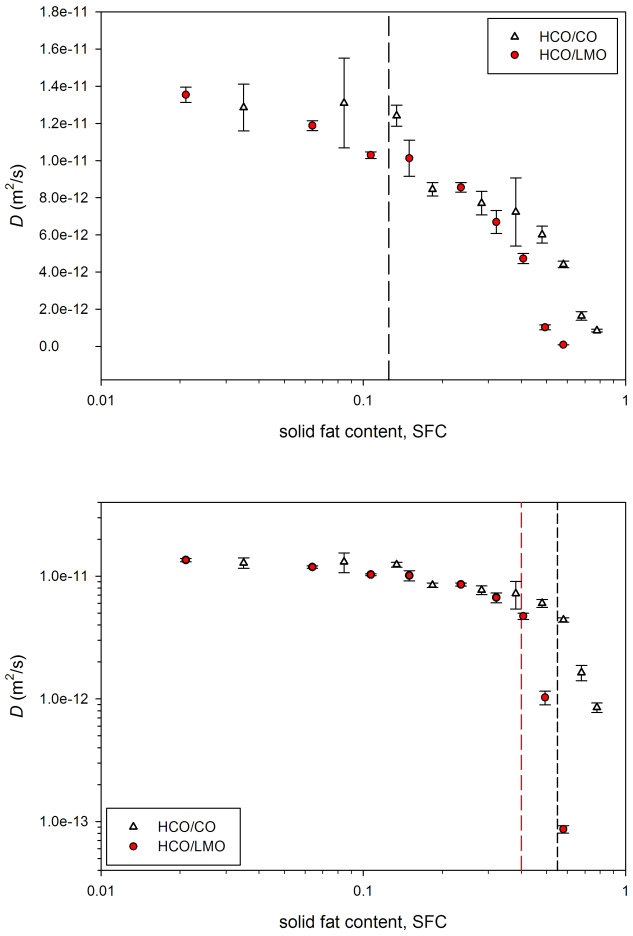

Fig. 3 Diffusion coefficient as a function of solid fat content for HCO/LMO and HCO/CO samples. Error bars are averaged over three FRAP experiments. Dashed lines mark observed SFC transition values that are detailed in the text.

1.75×10^{-11} m^2/s for LMO. Via the Stokes-Einstein equation $D_0 = k_BT/f$, where k_B is the Boltzmann constant and T is the absolute temperature, and the two oils have similar friction factors f. We separately measured each viscosity at 25°C to be 56.9 ± 1.2 mPa·s for CO and 43.4 ± 1.1 mPa·s for LMO. The LMO molecules are *n*-alkanes predominantly 22 – 30 carbons in length with an average molecular weight (MW) of 394 g/mole.[28] CO molecules are TAGs consisting of primarily unsaturated fatty acids, typically 18 carbons in length, esterified to a glycerol backbone (MW$\sim$ 930 g/mol). The two oils having comparable diffusivities despite the difference in MW can be explained by different shapes of the diffusing molecules, akin to the Mark-Houwink-Sakurada equation in polymer systems.[29] The CO molecule can be approximated as a sphere whereas the LMO molecule should be more of a prolate spheroid.

The frame rate was decreased over the recovery in order to avoid any bleaching during image capture, which can lead to slower calculated diffusion coefficients or be falsely interpreted as an immobile fraction.[30] As fluorescence intensity was fully recovered in all samples, we see no evidence of any samples having immobile fractions. This is contrary to prior work in food fat systems[6] that uses the difference in the normalized ROI intensity before bleaching and after recovery to calculate the immobile fraction.[31] Previously reported reported diffusion coefficients are lower than those we report, which we attribute to two reasons. First, the authors noted that their photobleaching step took 50 seconds, which was 4 – 85$\times$ longer than intensity recovery. This breaches the aforementioned 15:1 ratio between recovery and bleaching time[25] and likely results in bleaching of incoming dye. Also, authors used $\omega_B = 22$ µm and defined $\omega_{ROI} = 7.3$ µm; their difference was almost twice as large as that which we used. While $\omega_{ROI} < \omega_B$ is necessary to avoid edge effects, a greater difference between the two further violates the square-well intensity profile at $t = 0$, a necessary assumption for the solution to the diffusion equation. These two will likely lead to a lower calculated D.

Figure 3 shows the D values as a function of SFC for both HCO/CO and HCO/LMO. We found that D decreases with increasing SFC, which indicates that the oil and dye molecules were subject to pathways with dimensions of similar order of magnitude. These would likely occur in the primary building blocks of fat crystals, the nanoplatelets of TAG lamellae. Had such regions not allowed the passage of liquid oil, D would

be unaffected by increasing SFC, particularly at low SFC, much like small molecule diffusion through dilute solutions of impermeable obstructions.[32] Similarly, if the oil and dye molecules were much smaller than the liquid pathways, they would pass unhindered and D would be constant for all SFC values. While experiments up to 100 wt% added HCO were attempted, data beyond 80 wt% added HCO for the HCO/CO system and 70 wt% for the HCO/LMO system could not be collected because a single FRAP experiment took upwards of 8 hours. Such D measurements would be below our experimental sensitivity. We plot D vs. SFC on a lin-log plot in Figure 3, following similar FRAP work using polymer gel networks.[33] We also plot D vs. SFC on a log-log scale as per FRAP work in food systems.[19]

We expect a macroscopic transition at low SFC marking the critical concentration at which flocs, which themselves are made of primary crystal structures, begin overlapping. This would lead to network formation. We observe that using either CO or LMO, mixtures at and below 10% SFC flow as viscous liquids, whereas those at and above 20% SFC resist flow when inverted for several hours. At 15% SFC, no flow occurs over the timescale of a single FRAP experiment ($\sim$ 5 minutes). The critical overlap concentration for both of our systems is thus somewhere between 10-15% SFC. We mark 12.5% SFC in the lin-log plot of Figure 3 and note that it appears to mark a change in slopes, as the gel point in polymer systems.[33]

The value of the critical overlap concentration should be similar to the transition from the strong-link regime to the weak-link regime in the fractal model for colloidal gels,[34] which has been applied to fat crystal networks.[35,36] The strong-link range occurs at low SFC and is typified by the connections between primary crystal clusters dominating the observed bulk rheological behavior.[36,37] The strong to weak-link transition has been reported at particle concentrations of 10% for colloidal gels[34] and below 12% SFC for fat crystal networks.[38] The latter is very similar to our suggested range between 10-15% SFC. We verify via polarized light images at the lowest SFC, 5/95 (w/w), do show individual clusters and no greater network formation (see Figure 4). Interestingly, changing the oil leads to dissimilar microstructures. HCO crystal clusters in CO appear more diffuse and contain spindle-like crystals. This geometry will have a greater specific surface area and be more likely to interconnect creating a network structure at low SFC. Conversely, HCO crystallized in LMO yields slightly larger and more densely packed clusters with lower specific surface area. This difference in microstructure does not individualize the diffusivities of the two systems at low SFC. We speculate that diffusion at low SFC is dominated by the liquid oil regions, where oil and dye molecules should move more freely. If the flocs were both large and numerous enough to place the FRAP ROI solely on them, then the resulting local diffusion coefficient would be much smaller than a randomly located one.[39] However, the liquid area is on par with the ROI size, so differences in crystal floc and network structure between the two systems do not seem to affect the trend.

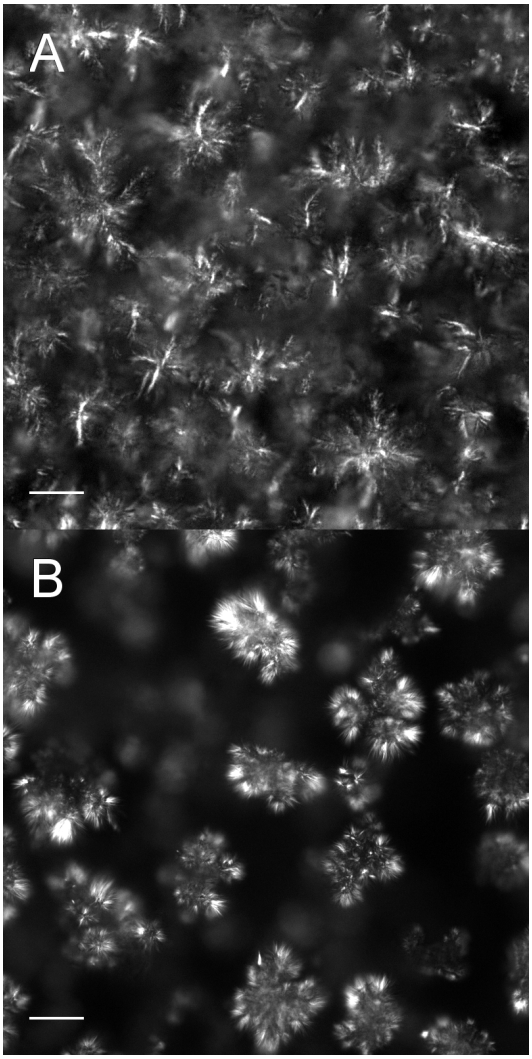

Fig. 4 Polarized light images of 5/95 (w/w) (A) HCO/CO and (B) HCO/LMO systems. Scale bars denote 30 μm. Images were captured on an inverted light microscope.

From the log-log plot of Figure 3, a second, higher SFC transition is apparent. This transition appears around 40% SFC for HCO/LMO and 55% SFC for HCO/CO, both of which we mark in Figure 3. Here, diffusion is heavily influenced by the fat crystals and few oil and dye molecules can diffuse unimpeded. Indeed, Figure 6 shows that sparse regions of liquid oil seem to exist only at the boundaries between large interconnected flocs. Nonspherical diffusant probes,[40] larger probe sizes,[41] and smaller pore cross-sectional areas[39] will all independently reduce calculated D values, provided that the

latter two are of the same order of magnitude. In our experiments, we suggest that the crystal structure is most responsible for the reduced D values in the HCO/LMO system. While the differences in microstructure are always present, it is at this higher transition that they dominate the contribution to D.

We use WAXD to verify the polymorphic form. We expect all blends to be in the β polymorphic form as, when blended with liquid oil, HCO has been shown to yield the most stable β polymorph.[42] Our WAXD results (Figure 5) are consistent with this, exhibiting the three characteristic β peaks at d-values at 0.46 nm, 0.39 nm, and 0.37 nm. Thus, the deviation in D between the two systems at high SFC values cannot be attributed to differences in polymorphic form. We use SAXD to calculate the nanoplatelet length via Equation 5. At the nanoscale, it has been reported that, for a fixed cooling rate, fat crystal nanoplatelet length can vary with changes in added solid fat via changes in local viscosity or modifications in TAG fatty acid composition.[42,43] It may also be possible that the different oils lead to differences in crystal thickness, as seen in the crystalline regions of polymer gels.[44] We thus calculated the nanoplatelet thickness using the Scherrer equation from the (001) SAXD peaks at $d = 4.42$ nm. We find no statistically significant differences in thickness between any of the systems, so the nanoplatelet thickness is diffusion-limited.

We now expand on the SFC transition points of Figure 3. While the critical overlap concentration, marking the start of network formation, has been studied in many food fat crystals,[35,36,38] the higher transition has not been reported in these systems. Similar second concentration-based transitions have been shown in starches,[19] biopolymers,[45] and polymers.[46,47] Polymer networks are divided into three regimes: dilute, semidilute, and concentrated. The semidilute and concentrated regimes can further be divided into unentangled and entangled regions that are dependent on polymer MW, but for the purpose of this work we focus on low MW in which the entanglement crossover point occurs after the system enters the concentrated regime.[48] Dilute polymer solutions consist of isolated polymer blobs characterized by the polymer radius of gyration, r_G. A small diffusing molecule in a dilute polymer solution will probe the bulk macrorheological properties.[49] At semidilute concentrations, polymer chains begin to overlap and create a mesh with void dimension (correlation length) ξ that decreases with increasing concentration. This dilute-semidilute transition is typically referred to as c^*. Probes smaller than r_G will, beyond c^*, measure the local rheological properties that differ from the bulk measurements. We suggest that the critical overlap concentration at low SFC values is the fat crystal analogue of c^*. The concentrated polymer regime is typified by indistinguishable polymer density fluctuations at any given location and constant polymer chain dimensions.[50] We propose that the this is the point where crystallization kinetics become diffusion-limited, and fat crystal

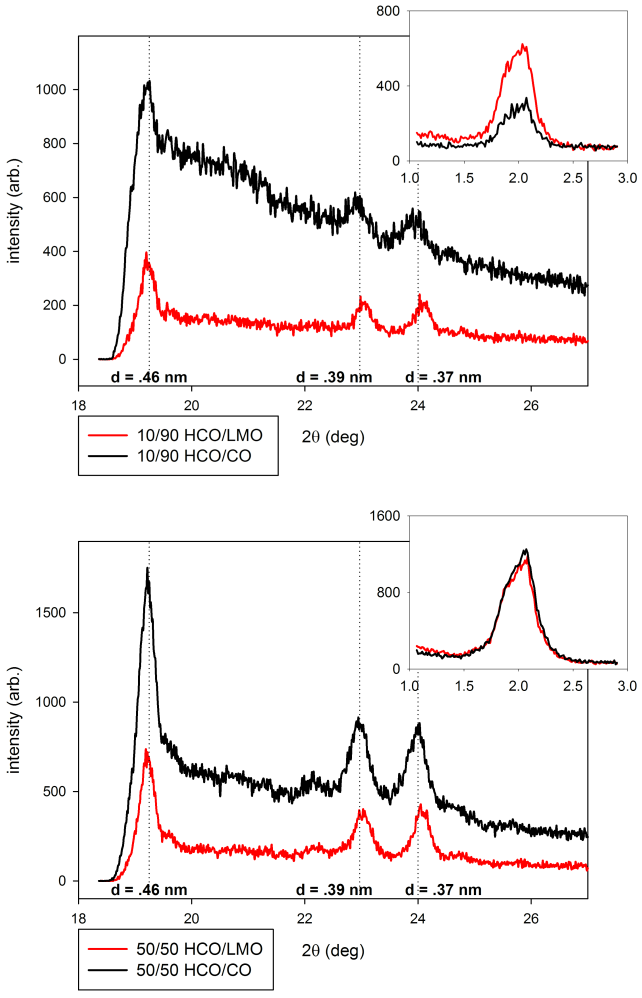

Fig. 5 SAXD (insets) and WAXD results at low (10/90) and high (50/50) weight fractions of added HCO. WAXD peaks are labeled with d-values indicative of β polymorphic form.

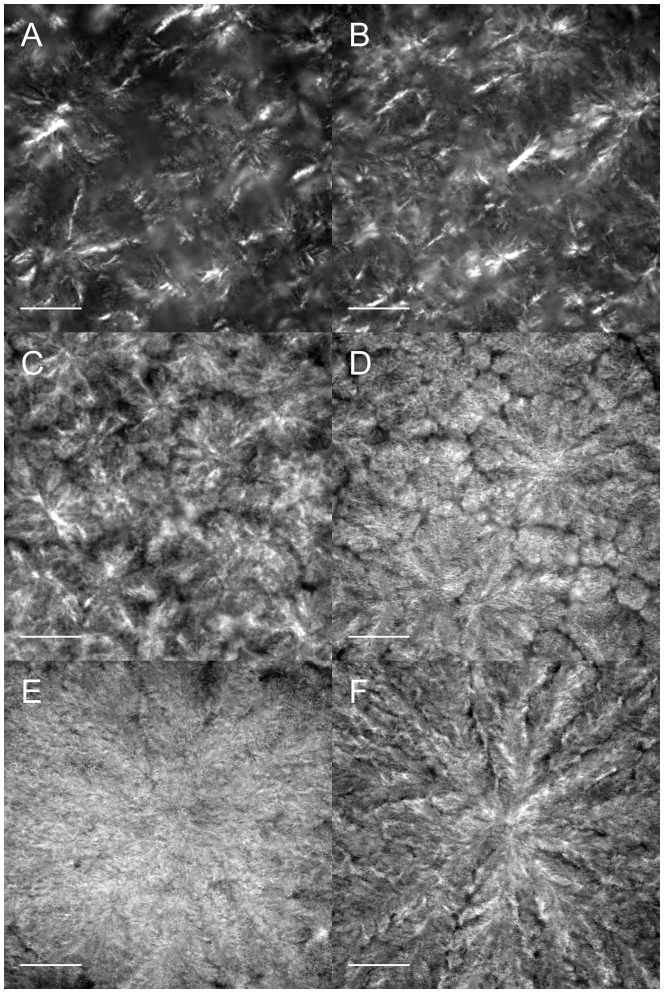

Fig. 6 Polarized light images of (top to bottom row) 10/90, 50/50, and 70/30 (w/w) samples of HCO/LMO (left) and HCO/CO (right) systems. Crystalline regions appear bright while liquid oil appears dark. Scale bars denote 30 μm.

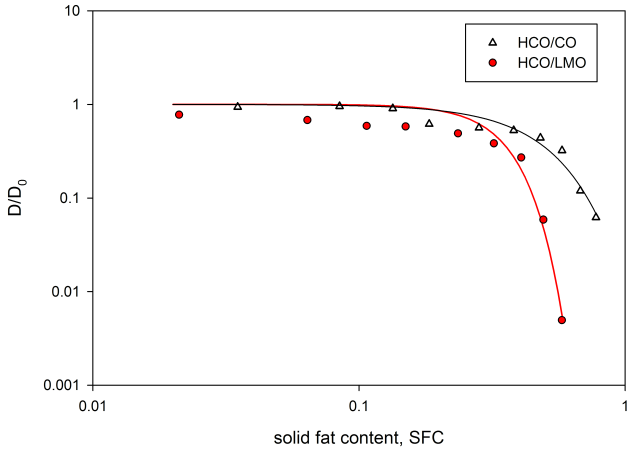

Fig. 7 Normalized diffusion coefficients as a function of SFC. Lines are corresponding best fits to the stretched exponential for each data set.

fractal sizes reach a constant value. Constant fractal dimensions have been reported at SFC values in this range.[38] Our oil and dye tracers, being smaller than cluster dimensions, are able to probe the local diffusivity at the entire range of SFC values examined.

Given the similarities to polymer networks, we now interpret the observed relationship between D and SFC using prior work in polymer systems, again assuming the matrix concentration, a typical independent variable, is equivalent to SFC. There exist many theoretical models that differ depending on the way they approximate both the diffusant molecule and the continuous matrix.[51,52] One of the most agreed-upon fits is the phenomenological stretched exponential fit, $D = D_0 \exp(-\alpha c^{\nu})$, where c is polymer concentration and α and ν are fitting parameters.[53] This fit has been used extensively and shown to fit over a wide range of polymer concentrations.[41,46,47] Our data can also be approximated by a stretched exponential fit, using SFC instead of c, as shown in Figure 7. A modified form, $D = D_0 \exp(-b(r/\xi)^a)$, has been shown to collapse data to a single curve.[49] Here, r is the probe radius, $\xi = r_G (c/c^*)^{-n}$, and n describes the solvent quality. There are no fat crystal analogues for n, though the different microstructures of Figure 4 suggest that such a parameter may be warranted. The possibility of a similar master curve for fat-based systems has exciting implications in predicting the effects on oil migration that changing the sizes and interactions of the components as well as the processing conditions may have.

4 Conclusions

We have used FRAP to calculate the local diffusion coefficients of HCO in both CO and LMO at a range of SFCs. Differences in molecular similarity lead to disparate crystal cluster structures, though the polymorphic form and nanoplatelet thicknesses for all samples remain the same. Intermolecular interactions are shown to affect crystal structure on the microscale, yet the resulting diffusion coefficients are indistinguishable at low SFC. Here the void space is vast and the diffusant size is small, so the measurements are of the bulk macrorheology, akin to the dilute region of a polymer solution. Both systems exhibit a crossover SFC in the range of $10-15\%$, which we relate to the overlapping of individual crystal clusters. We connect this to the overlap concentration c^* and the start of the semidilute regime associated with polymer network formation. There exists a second transition

$\sim$ 40% SFC for HCO/LMO (55% for HCO/CO) that marks the point at which our small diffusant molecules are measuring the nanorheological properties of the system, and differences in crystal dimensions at the nanoscale must be taken into account. This region matches well with the concentrated regime of polymer networks in which polymer chain dimensions are no longer concentration-dependent. We suggest that fat crystal fractal sizes become diffusion-limited at this point. The full relationship can be approximated by the stretched exponential model commonly used in polymer matrix models, indicating that additional studies are merited to further explore the applicability of polymer gelation models in food fat systems.

5 Acknowledgments

Funding from the Natural Sciences and Engineering Research Council of Canada as well as the Ontario Ministry of Research and Innovation is acknowledged.

References

1 V. Ghosh, G. R. Ziegler and R. C. Anatheswaran, *Critical Reviews in Food Science and Nutrition*, 2002, **42**, 583–626.
2 P. Lonchampt and R. W. Hartel, *European Journal of Lipid Science and Technology*, 2004, **106**, 241–274.
3 J. M. Aguilera, M. Michel and G. Mayor, *Journal of Food Science*, 2004, **69**, R167–R174.
4 M. E. Miquel, S. Carli, P. J. Couzens, H.-J. Wille and L. D. Hall, *Food Research International*, 2001, **34**, 773–781.
5 Y. J. Choi, K. L. McCarthy and M. J. McCarthy, *Journal of Food Science*, 2005, **70**, E312–E317.
6 S. Marty, M. Schroeder, K. W. Baker, G. Mazzanti and A. G. Marangoni, *Langmuir*, 2009, **25**, 8780–8785.
7 K. W. Smith, F. W. Cain and G. Talbot, *Food Chemistry*, 2007, **102**, 656–663.
8 T. Motwani, W. Hanselmann and R. C. Anantheswaran, *Journal of Food Engineering*, 2011, **104**, 186–195.
9 R. S. Khan and D. Rousseau, *European Journal of Lipid Science and Technology*, 2006, **108**, 434–443.
10 T. S. Omonov, L. Bouzidi and S. S. Narine, *Chemistry and Physics of Lipids*, 2010, **163**, 728–740.
11 F. Maleky and A. G. Marangoni, *Soft Matter*, 2012, **7**, 6012–6024.
12 H. Dahlenborg, A. Millqvist-Fureby, B. Bergenståhl and D. J. Kalnin, *Journal of the American Oil Chemists' Society*, 2011, **88**, 773–783.
13 H. Dahlenborg, A. Millqvist-Fureby, B. D. Brandner and B. Bergenståhl, *European Journal of Lipid Science and Technology*, 2012, **114**, 919–926.
14 G. Ziegleder, C. Moser and J. Geier-Greguski, *Fett-Lipid*, 1996, **96**, 196–199.
15 D. Axelrod, D. E. Koppel, J. Schlessinger, E. Elson and W. W. Webb, *Biophysical Journal*, 1976, **16**, 1055–1069.
16 G. Carrero, E. Crawford, M. Hendzel and G. de Vries, *Bulletin of Mathematical Biology*, 2004, **66**, 1515–1545.
17 B. L. Sprague and J. G. McNally, *Trends in Cell Biology*, 2005, **15**, 84–91.
18 J. G. McNally, *Methods in Cell Biology*, 2008, **85**, 329–351.
19 P. P. Perry, M. A. Fitzgerald and R. G. Gilbert, *Biomacromolecules*, 2006, **7**, 521–530.
20 J. Floury, M.-N. Madec, F. Waharte, S. Jeanson and S. Lortal, *Food Chemistry*, 2012, **133**, 551–556.
21 J. V. C. Silva, P. D. S. Peixoto, S. Lortal and J. Floury, *Journal of Dairy Science*, 2013, **96**, 6186–6198.
22 L. Svanberg, L. Ahrné, N. Lorén and E. Windhab, *Procedia Food Science*, 2011, **1**, 1910–1917.
23 L. Svanberg, L. Ahrné, N. Lorén and E. Windhab, *Food Research International*, 2011, **44**, 1339–1350.
24 J. Hagman, N. Lorén and A.-M. Hermansson, *Biomacromolecules*, 2010, **11**, 3359–3366.
25 T. K. L. Meyvis, S. C. De Smedt, P. Van Oostveldt and J. Demeester, *Pharmaceutical Research*, 1999, **16**, 1153–1162.
26 K. Braeckmans, L. Peeters, N. N. Sanders, S. C. De Smedt and J. Demeester, *Biophysical Journal*, 2003, **85**, 2240–2252.
27 A. G. Marangoni and L. H. Wesdorp, *Structure and Properties of Fat Crystal Networks*, CRC Press, Boca Raton, FL, USA, 2nd edn, 2013.
28 S. Haj-Shafiei, *MSc thesis*, Ryerson University, 2011.
29 I. Teraoka, *Polymer Solutions: An Introduction to Physical Properties*, John Wiley & Sons, Inc., New York, USA, 2002.
30 J. Wu, N. Shekhar, P. P. Lele and T. P. Lele, *PLoS ONE*, 2012, **7**, e42854.
31 E. D. Siggia, J. Lippincott-Schwartz and S. Bekiranov, *Biophysical Journal*, 2000, **79**, 1761–1770.
32 L. Petit, C. Barentin, J. Colombani, C. Ybert and L. Bocquet, *Langmuir*, 2009, **25**, 12048–12055.
33 F. Di Lorenzo and S. Seiffert, *Macromolecular Chemistry and Physics*, 2014, **215**, 2097–2111.
34 W.-H. Shih, W. Y. Shih, S.-I. Kim, J. Liu and I. A. Askay, *Physical Review A*, 1990, **42**, 4772–4779.
35 A. G. Marangoni and D. Rousseau, *Journal of the American Oil Chemists' Society*, 1999, **73**, 991–994.
36 S. S. Narine and A. G. Marangoni, *Food Research International*, 1999, **32**, 227–248.
37 D. Tang and A. G. Marangoni, *Trends in Food Science &*

Technology, 2007, **18**, 474–483.
38 T. S. Awad, M. A. Rogers and A. G. Marangoni, *Journal of Physical Chemistry B*, 2004, **108**, 171–179.
39 S. Wassén, R. Bordes, T. Gebäck, D. Bernin, E. Schuster, N. Lorén and A.-M. Hermansson, *Soft Matter*, 2014, **10**, 8276–8287.
40 B. Jönsson, H. Wennerström, P. G. Nilsson and P. Linse, *Colloid& Polymer Science*, 1986, **264**, 77–88.
41 A. Michelman-Ribeiro, F. Horkay, R. Nossal and H. Boukari, *Biomacromolecules*, 2007, **8**, 1595–1600.
42 F. Maleky, N. C. Acevedo and A. G. Marangoni, *European Journal of Lipid Science and Technology*, 2012, **114**, 748–759.
43 N. C. Acevedo and A. G. Marangoni, *Crystal Growth & Design*, 2010, **10**, 3334–3339.
44 P.-D. Hong, J.-H. Chen and H.-L. Wu, *Journal of Applied Polymer Science*, 1998, **69**, 2477–2486.
45 M. Nydén and O. Söderman, *Macromolecules*, 1998, **31**, 4990–5002.
46 R. Liu, X. Gao, J. Adams and W. Oppermann, *Macromolecules*, 2005, **38**, 8845–8849.
47 T. Cherdhirankorn, A. Best, K. Koynov, K. Peneva, K. Muellen and G. Fytas, *Journal of Physical Chemistry B*, 2009, **113**, 3355–3359.
48 D. Wöll, *RSC Advances*, 2014, **4**, 2447–2465.
49 R. Holyst, A. Bielejewska, J. Szymański, A. Wilk, A. Patkowski, J. Gapiński, A. Żywociński, T. Kalwarczyk, E. Kalwarczyk, M. Tabaka, N. Ziębacz and S. A. Wieczoreka, *Physical Chemistry Chemical Physics*, 2009, **11**, 9025–9032.
50 W. W. Graessley, *Polymer*, 1980, **21**, 258–262.
51 B. Amsden, *Macromolecules*, 1998, **31**, 8382–8395.
52 L. Masaro and X. X. Zhu, *Progress in Polymer Science*, 1999, **24**, 731–775.
53 G. D. J. Phillies, *Macromolecules*, 1986, **19**, 2367–2376.

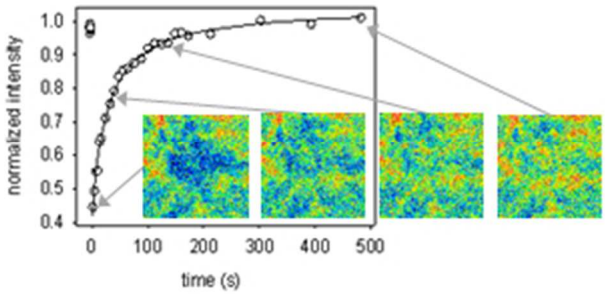

79x39mm (96 x 96 DPI)